Turbulence power laws and inverse motion modeling in images

Patrick Héas, Etienne Mémin, Dominique Heitz, Pablo D. Mininni

INSTITUT NATIONAL DE RECHERCHE EN INFORMATIQUE ET EN AUTOMATIQUE

Turbulence power laws and inverse motion modeling in images

Patrick Héas [1] — Etienne Mémin [1] — Dominique Heitz[2] — Pablo Mininni[3]

[1]INRIA Bretagne Atlantique Research Center, Rennes, France; [2] Cemagref, Rennes, France; [3] Departamento de Fisica, UBA

- CONICET, Buenos Aires, Argentina

N° 6948

Mai 2009

Thèmes COG et NUM

ISSN 0249-6399 ISRN INRIA/RR--6948--FR+ENG

Turbulence power laws and inverse motion modeling in images

Patrick Héas [1] , Etienne Mémin [1] , Dominique Heitz[2] , Pablo Mininni[3]

[1]INRIA Bretagne Atlantique Research Center, Rennes, France; [2] Cemagref, Rennes, France; [3] Departamento de Fisica, UBA - CONICET, Buenos Aires, Argentina

Thèmes COG et NUM — Systèmes cognitifs et Systèmes numériques
Projet Fluminance

Rapport de recherche n° 6948 — Mai 2009 — 38 pages

Abstract: Based on scaling laws describing the statistical structure of turbulent motion across scales, we propose a multiscale and non-parametric regularizer for the estimation of velocity fields of bidimensional or quasi bidimensional flows from image sequences. Spatial regularization principle used in order to close the ill-posed nature of motion estimation is achieved by constraining motion increments to behave through scales as the most likely self-similar process given some image data. In a first level of inference, the estimation formulated as a hard constrained minimization problem is optimally solved by taking advantage of lagrangian duality. It results in a collection of first-order regularizers acting at different scales. This estimation is non-parametric since the optimal regularization parameters at the different scales are obtained by solving the dual problem. In a second level of inference, the most likely self-similar model given the data is optimally selected by maximization of bayesian evidence. The motion estimator accuracy is first evaluated on a synthetic image sequence of simulated bidimensional turbulence and then on a real meteorological image sequence. Results obtained with the proposed physical based approach exceeds the best state of the art results. Furthermore, selecting from images the most evident multiscale motion model enables the recovery of physical quantities which are of major interest for turbulence characterization.

Key-words: Motion estimation; regularization; self-similarity; bayesian inference; variational methods; turbulence

Unité de recherche INRIA Rennes
IRISA, Campus universitaire de Beaulieu, 35042 Rennes Cedex (France)
Téléphone : +33 2 99 84 71 00 — Télécopie : +33 2 99 84 71 71

Résumé : Pas de résumé

Mots-clés : Pas de motclef

1 Introduction

Images constitute important data for studying fluid flows since they can characterize a large range of spatial scales in comparison to sparse information provided by standard point measurement techniques.

Indeed, flow visualization has been a powerful tool to depict or to understand flow feature properties. Efforts to develop high-quality flow visualization techniques date back over a century. The analysis of the recorded images consisted firstly to a qualitative interpretation of the streak lines leading to an overall global insight into the flow properties but lacking quantitative details on important parameters such as velocity fields. Point measurement tools such as Hot Wire Anemometry (HWA) or Laser Doppler Velocimetry have typically provided these details. Since these probes give information only at the point were they are placed, simultaneous evaluations at different points require to dispose a very large number of probes, leading to complicated experiments. For instance, HWA experiments allow the production of both a spatial field and a pseudo-spatial field using Taylor's approximation of frozen flow. In an effort to cope with limitations of point wise velocity measurements techniques, Particle Image Velocimetry (PIV), a non-intrusive image-based diagnostic approach, has been developed in the last two decades. PIV techniques[1] enable the obtention of velocity fields by seeding the flow with particles (*e.g.* dye, smoke, particles) and retrieving the motion of these tracers by inverse modeling.

Correlation-based techniques are common inverse approaches to extract sparse velocity fields from image sequences considering an uniformity assumption over a spatial window and a preservation of the brightness of the tracer along its trajectory (Adrian, 1991; Raffel *et al.*, 2007). These PIV methods have demonstrated their robustness and accuracy for velocity measurement. However, the brightness preservation hypothesis inherent to the method is often not adapted to the data (*e.g.* scalar diffusion, three-dimensional effects). Moreover, the assumption of motion spatial uniformity give rise in essence to an intrinsic measurement scale bound corresponding the correlation window size. This measurement scale bound, which is often ignored in the analysis of the extracted velocity fields, is in most case greater than the smallest motion scale observed in the images. In particular, for low-contrasted observations such as scalar images, correlation-based methods are considerably limited and provide only very sparse motion fields.

[1] We denote by PIV techniques all the inverse motion modeling methods based on particle images, including correlation-based techniques and optic-flow methods.

In computer vision, estimating the projected apparent motion of a three-dimensional scene onto the image plane, refereed in the literature as optical-flow, has been an intensive subject of researches since the 80s and the work of Horn & Schunck (1981). The inverse motion modeling proposed in this seminal work is formulated in a differential scheme which enables the introduction of physical-based direct observation model (relying on brightness preservation, mass conservation, scalar transport, ...) adpated to the image data (Fitzpatrick, 1988; Heas *et al.*, 2007; Heas & Memin, 2008; Liu & Shen, 2008). The direct model links at each point a motion vector to the image intensity function. Let us note that there exist global spatial polynomial models of the motion field which can consistute an alternative to a dense description (Cuzol & Memin, 2007). However, these models are insufficient for fluid flows since small scales are hardly represented. For dense motion representations, regularization models are required to remove the motion ambiguities and achieve inversion. But actual regularizers are all insufficient since they impose in a small spatial neighborhood a prior smoothness which describes improperly the regularity of fluid flows. Moreover they depend on a tuning parameter weighting the amount of smoothing required to cure the ill-posed nature of the direct observation model used in the inverse motion problem. For large or small values of this parameter, which is almost unavoidable when facing noisy images or with low photometric contrasts, the solution tends to be too smooth or too noisy and presents sometimes a lack of accuracy at large scales.

Nevertheless, it is possible to overcome these limitations. Firstly, important advances have been achieved in statistical modeling of turbulence since the precursor work of *Kolmogorov* in 1941 (Kraichnan, 1967; Frisch, 1995; Lindborg & Cho, 2001). In particular, it has been shown from the Navier-Stokes equations for different kind of flows that turbulent motion regularity can be characterized using some (assumed universal) scaling properties of the Probability Distribution Function (PDF) of motion increments. Secondly, bayesian modeling provides a reliable framework for the design of non-parametrical methods and for selecting the regularization model given some data (Gull, 1989; MacKay, 1992; Jaynes, 2003). Due to the limitation of correlation-based techniques to include direct observation models, and due to their inherent discrete and local nature which makes difficult the incorporation of a prior global physical regularity, we rather focus on differential optical flow methods and the bayesian framework. Therefore, this work exploits simultaneously two ideas: the use of turbulence scaling laws for motion regularization in optic-flow inverse problems; and the selection by bayesian evidence maximization of the most appropriate scaling law model describing the image intensity function based on a variable hierarchy linking 'image' to 'motion' to 'scaling laws'. The resulting regularization is built from the physics of fluids. It is multiscale as it controls the solutions within a prescribed scale range. It is also non-parametric in the sense that it does not involve the tuning of any parameters. Finally, it allows the recovering of some important

quantities for turbulence characterization such as energy flux across scales.

The regularization model presented in this work is generic and designed for various fluid imaging methods. It does not restrict to single particle images. Indeed, inverse motion modeling is needed for the analysis by satellite imagery of geophysical flows or for the study by Schlieren velocimetry of experimental flows, among other velocimetry methods commonly used in laboratory.

The paper is organized as follows. In section 2, we briefly overview optic-flow methods and review the motion scaling properties developed in theoretical works on turbulence. Then, in section 3, self-similar regularizers are introduced which induce the resolution of a multiscale constraint minimization problem. Using bayesian evidence, section 4 proposes the optimal selection of the prior self-similar model. Finally, synthetic and real world experiments on meteorological image data are presented.

2 Related work

2.1 Optic-flow methods

Image observation model Motion perceived through image intensity $I(\mathbf{s},t)$ variations and the projection on the image plane of the real underlying velocity field $\mathbf{v}=(u,v)$ are identical when considering rigid motion and stable lighting conditions. In this situation, motion $\mathbf{v}$ respects the standard Optical Flow Constraint (OFC) equation which reads:

$$\frac{dI}{dt}=\frac{\partial I}{\partial t}+\nabla I\cdot\mathbf{v}=0. \tag{1}$$

For fluids, this observation model remains valid in the theoretical case of bidimensional incompressible flows. Nevertheless, these flows are relevant for many geophysical applications studying quasi bidimensional flows, as *e.g.* meteorology and oceanography (J.Pedlosky, 1987). Based on mass conservation, the integrated continuity equation has been proposed in the literature for various three-dimensional fluid flows visualized in a projected image plane in order to link the image intensity function I to a vertically averaged horizontal velocity field $\mathbf{v}$ (Fitzpatrick, 1988; Corpetti *et al.*, 2002; Heas *et al.*, 2007):

$$\frac{\partial I}{\partial t}+\nabla I\cdot\mathbf{v}+I\mathrm{div}\,\mathbf{v}=0. \tag{2}$$

However, these observation models remain underconstrained, as they provide only one equation for two unknowns (u,v) at each spatio-temporal location $(\mathbf{s},t)$.

Standard regularization To deal with this underconstrained estimation problem, the most common setting consists in enforcing some spatial coherence. This coherence is imposed either globally through a regularization functional defined over the whole image domain Ω or locally relying on polynomial models defined on local bounded supports. Global regularization schemes are convenient to model global coherence via local spatial dependencies. More precisely, the estimation is performed through the minimization of an energy functional composed of two terms:

$$f(I, \mathbf{v}) = f_d(I, \mathbf{v}) + \alpha f_r(\mathbf{v}). \tag{3}$$

The first one $f_d(I, \mathbf{v})$, the data term, penalizes discrepancies from the observation models. For example, discretizing in time the OFC equation result in the data term:

$$f_d(I, \mathbf{v}) = \frac{1}{2}\int_\Omega (\tilde{I} - I + \mathbf{v} \cdot \nabla \tilde{I})^2 d\mathbf{s} \tag{4}$$

where $\tilde{I}$ denotes the image $I(t + \Delta t)$. The second component $f_r(\mathbf{v})$, the regularization term, acts as a spatial *prior* enforcing the solution to follow some smoothness properties. In the previous expression, $\alpha > 0$ denotes a regularization parameter controlling the balance between the smoothness and the global adequacy to the observation model. In this framework, Horn & Schunck (1981) proposed a first-order regularization of the two spatial components u and v of velocity field $\mathbf{v}$:

$$f_r(\mathbf{v}) = \frac{1}{2}\int_\Omega (||\nabla u||^2 + ||\nabla v||^2) d\mathbf{s} \tag{5}$$

However, motion gradient penalization is not adapted to fluid flows as it comes to penalize in an homogeneous way the curl and the divergence of the solution. Second order regularizers on motion vorticity and divergence have been proposed to overcome such limitations (Corpetti *et al.*, 2002, 2006). Regularizations including additional constraints on vanishing divergence have also recently been proposed (Yuan *et al.*, 2007). All these approaches depend however on the tuning of α and only mimic qualitatively physical behavior but are not precisely related to the physics of fluid motion.

Multi-resolution approach A major problem with differential observation models is the estimation of large displacements. Indeed, these equations are only valid if the solution remains in the region of linearity of the image intensity function. A standard approach for tackling non-linearity is to rely on a Gauss-Newton strategy which consists in applying successive linearizations around a current estimate and

to warp a multi-resolution representation of the data accordingly (Bergen *et al.*, 1992). More explicitly, a large displacement field $\tilde{\mathbf{v}}$ is first estimated with the original data term at coarse resolution, where the linearity assumption is valid. Then, introducing the decomposition:

$$\mathbf{v} = \tilde{\mathbf{v}} + \mathbf{v}', \tag{6}$$

motion is refined through an incremental fields $\mathbf{v}'$ estimated using a linearized motion-compensated data term while going down the resolution levels of an image pyramid and projecting motion on the current level through duplication or spline interpolation methods (Unser, 1999). For example, the linearization around $\tilde{\mathbf{v}}(\mathbf{s})$ of the displaced frame difference (which relies on the assumption of brightness conservation along the trajectory):

$$I(\mathbf{s} + \mathbf{v}(\mathbf{s}), t + \Delta t) - I(\mathbf{s}, t) = 0, \tag{7}$$

yields the linearized OFC data term:

$$f_d(I, \mathbf{v}) = \frac{1}{2} \int_\Omega \left(\tilde{I}(\mathbf{s}) - I(\mathbf{s}, t) + \mathbf{v}'(\mathbf{s}) \cdot \nabla \tilde{I}(\mathbf{s}) \right)^2 d\mathbf{s}, \tag{8}$$

where $\tilde{I}(\mathbf{s}) = I(\mathbf{s} + \tilde{\mathbf{v}}(\mathbf{s}), t + \Delta t)$ denotes the motion compensated image. Let us remark that for points $\mathbf{s} + \tilde{\mathbf{v}}(\mathbf{s})$ outside of the pixel grid, the construction of $\tilde{I}(\mathbf{s})$ requires the use of interpolation functions such as splines. As suggested in Heas *et al.* (2007) and adapted by Heitz *et al.* (2008) for particle imagery, an alternative to the multiresolution setup would consist to rely on sparse motion fields provided by traditional correlation-based techniques (thus corresponding to a large scale estimate) and to interpolate these sparse velocities using the proposed self-similar regularization.

Minimization issues In order to achieve the functional minimization, the associate Euler-Lagrange equations are classically solved. Another common approach is to perform a direct discretization of the functional yielding a well-known Markov Random Field (MRF) problem formulation. In both cases, efficient deterministic optimization techniques (gradient descent methods, multi-grid algorithms, etc) can be employed for convex functionals to access to the global minimum.

2.2 Turbulence statistical modeling

Since *Kolmogorov*'s works, turbulent motion increments have been known to be structured as nearly scale invariant spatial processes. To review turbulence models, let us define the longitudinal velocity increment function in the direction of a unitary vector $\boldsymbol{n}$ by:

$$\delta v_{\|}(\ell, \mathbf{s}, \boldsymbol{n}) = (\mathbf{v}(\mathbf{s} + \ell\boldsymbol{n}) - \mathbf{v}(\mathbf{s})) \cdot \boldsymbol{n}, \tag{9}$$

where the scalar ℓ represents a spatial increment. As a classical hypothesis in turbulence studies, we assume homogeneity and isotropy, that is to say we consider that the statistical properties of the velocity field are invariant under translation of spatial location $\mathbf{s}$ and rotation of direction θ[2]. In agreement with these assumptions, index to $\mathbf{s}$ and θ can be dropped and moments of the PDF of velocity increments $p_\ell(\delta v_{\|})$, the structure functions, can be approached by spatial integration:

$$\begin{aligned} \mathrm{E}[\delta v_{\|}(\ell)^p] &= \int_{\mathbb{R}} \delta v_{\|}(\ell)^p p_\ell(\delta v_{\|}(\ell)) d\delta v_{\|}(\ell) \\ &\approx \frac{1}{2\pi|\Omega|} \int_{\Omega} \int_{[0,2\pi]} \Big(\delta v_{\|}(\ell, \mathbf{s}, \theta)\Big)^p d\theta \, d\mathbf{s}, \end{aligned} \tag{10}$$

where $|\Omega|$ denotes the spatial domain area.

For three-dimensional isotropic turbulent flows, Kolmogorov (1941) demonstrated from the Navier-Stokes equations that the third order moment of the PDF $p_\ell(\delta v_{\|})$, namely the third order structure function, is linear w.r.t scale and follows the well-known "4/5 law" : $\mathrm{E}[\delta v_{\|}(\ell)^3] = -\frac{4}{5}\epsilon\ell$ in a so-called *inertial range* (see also Frisch (1995) for details on this demonstration). The inertial range is defined as $[\eta, \ell_0]$, where η represents the largest molecular dissipative scale and where ℓ_0 is much smaller than the diameter L of the largest vortex. Within this range, an energy flux cascades from large to small scales. The kinetic energy dissipation rate ϵ corresponds to this energy flux passed across scales which is then evacuated at small scales by molecular viscosity.

Analogously, for pure bidimensional turbulence with energy injection at scale ℓ_0, Kraichnan (1967) showed that there exist two different cascades: a direct cascade where $\mathrm{E}[\delta v_{\|}(\ell)^3] = \frac{1}{8}\epsilon_\omega \ell^3$ within the inertial range $[\eta, \ell_0]$, and an inverse cascade where $\mathrm{E}[\delta v_{\|}(\ell)^3] = \frac{3}{2}\epsilon\ell$ within range $[\ell_0, L]$. An enstrophy flux ϵ_ω (L^2 norm of vorticity) passes in the direct cascade from large to small scales, whereas an energy flux ϵ passes in the inverse cascade from small to large scales.

Concerning atmospheric turbulence, there are still open questions on the observed scaling laws. Lindborg (1999) and Lindborg & Cho (2001) proposed an answer to the question: "can atmospheric flow statistics be explained by two-dimensional turbulence?". These authors showed that the self-similar processes

[2]The hypothesis of isotropy can be relaxed, see e.g. Taylor *et al.* (2003). The method to recover isotropic statistics described there motivates the use of different directions for the displacements in Section 3.1

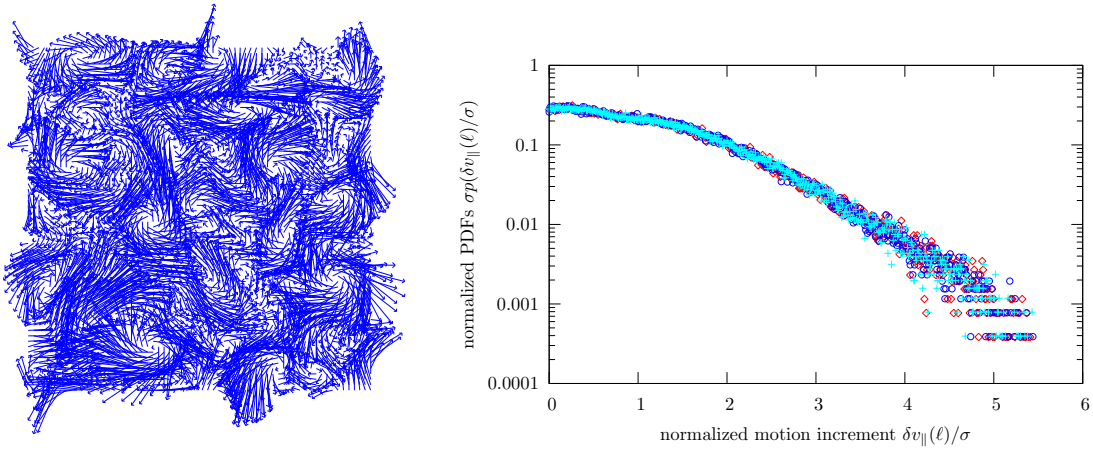

Figure 1: ***Bidimensional turbulent motion and similarity through scales of the normalized motion increment PDFs*** $\sigma_\ell p_\ell(\frac{\delta v_{\|}(\ell)}{\sigma_\ell})$ ***for scale increment*** $\ell = 1, 2, 4$.

observed in aircraft data (Nastrom *et al.*, 1984) at small scales and at large scales could be modeled by the superposition of a three-dimensional direct energy cascade and a bidimensional direct enstrophy cascade so that:

$$\mathrm{E}[\delta v_{\|}(\ell)^3] = -\epsilon\ell + \frac{1}{8}\epsilon_\omega \ell^3. \tag{11}$$

Aside from the problems in the determination of the direction of the energy and enstrophy cascade in atmospheric turbulence, it should be mentioned that there are still several independent exact relations that hold for the third-order structure function and which predict power law behavior (Monin & Yaglom, 1971; Kurien *et al.*, 2000).

Going further, *Kolmogorov* assumed that the longitudinal velocity increment functions were *strictly self-similar* processes. In this case the normalized PDF of motion increments is self-similar through scales as illustrated in figure 1. This implies that, in a given cascade, the p-th order structure function follows a power law:

$$\beta_p \ell^{\zeta_p} \sim \mathrm{E}[\delta v_{\|}(\ell)^p] = \mathrm{E}[\delta v_{\|}(\ell)^3]^{\frac{p}{3}} \sim \beta \ell^{\frac{p\zeta_3}{3}}, \tag{12}$$

with universal exponents ζ_p depending on space dimension and where the factor β_p is a function of the energy flux ϵ or the enstrophy flux ϵ_ω. A corollary of the strictly self-similar assumption is that in the inertial range any three-dimensional turbulent flow has a uniform Lipschitz regularity of $\zeta_1 = 1/3$ while a bidimensional turbulent flow is characterized by $\zeta_1 = 1$ (*i.e.* is regular). However, it is now well known that *Kolmogorov* assumption deviates from reality because of intermittency (coherent structures appearing in turbulence). As a consequence, only *non-strict self-similarity* can in reality be assumed for turbulent flows. It results that deviations on exponent values can be expected for $p \neq 3$, although power law behavior in the inertial range still holds. Finally, any bidimensional or three-dimensional turbulent flow is regular in the dissipative range and using Taylor expansion we have $\mathrm{E}[\delta v_{\|}(\ell)^2] \sim \ell^2$ within $\ell \in [0, \eta]$.This general power law dependence motivates the use of self-similar priors for motion estimation as discussed in the next section.

3 Self-similar regularization of optic-flow

Besides providing a closure for motion estimation, self-similar priors can yield several benefits:

- first, they constitute physical sound regularizers for fluid motion;
- second, they provide intrinsic multi-scale prior models which structures motion across scales;
- third, they lead to non-parametric methods with no regularization parameter α.

3.1 Self-similar constraints

Let us first formalize the use of self-similar constraints for the specification of regularization functionals. Although it does not provide an exact prediction on scaling laws for non-strictly self-similar flows, we chose to use the second order structure function $\mathrm{E}[\delta v_{\|}(\ell)^2]$ because it constitutes a convenient quadratic constraint for our purpose. Nevertheless, in section 4 we take into account deviations from the predicted law by selecting the most likely scaling law defined by parameters (β, ζ) given the image data. $\mathrm{E}[\delta v_{\|}(\ell)^2]$ is an expectation which can be obtained by spatial integration over the image domain and over all directions as presented in Eq. 10. A self-similar constraint $g_\ell(\mathbf{v})$ is then defined at each scale ℓ as the difference

between the 2-nd order structure function and a given power law. Thus, an estimated motion field should respect the constraint:

$$g_\ell(\mathbf{v}) = \frac{1}{2}(\mathrm{E}[\delta v_\parallel(\ell)^2] - \beta\ell^\zeta) = 0, \tag{13}$$

for given scaling exponent ζ and factor β.

3.2 Constrained motion estimation problem

Referring to section 2.1, the minimization of the ill-conditionned optic-flow estimation problem reads:

$$(\hat{\mathbf{v}}) = \arg\min_{\mathbf{v}} f_d(I, \mathbf{v}). \tag{14}$$

Adding the self-similar constraints, we obtain the closed constraint optic-flow minimization problem:

$$\begin{cases} \min_{\mathbf{v}} \ f_d(I, \mathbf{v}), \ \ \mathbf{v}(\mathbf{s}) \in \mathbb{R} \\ \text{subject to the constraints:} \\ g_\ell(\mathbf{v}) = 0, \ \ \forall \ell \in \mathbf{I} \end{cases} \tag{15}$$

where $\mathbf{I}$ is the scale range of the given power law.

3.3 Discrete problem formulation

Let us now express the constraint problem in its discrete form. The derivatives $\nabla_{\mathbf{v}} f_d(I, \mathbf{v})$ related to any motion-compensated data term which is quadratic with respect to motion increments $\mathbf{v}'$ (*e.g.* model of Eq. 8) can be expressed in the matricial form $A_0\mathbf{v}' - b_0$, when discretized on an image grid $\mathbf{S}$ of m points with a finite difference scheme. The two discretized components of $\mathbf{v}' \in \mathbb{R}^n$ now represent a field of $n = 2m$ variables supported by the grid $\mathbf{S}$, A_0 is $n \times n$ symmetric positive-definite, $\mathbf{b}_0 \in \mathbb{R}^n$ represents a vector of size n. The discrete data term can be rewritten as:

$$f_d(I, \mathbf{v}) = \frac{1}{2}\mathbf{v}'^T A_0 \mathbf{v}' - \mathbf{b}_0^T \mathbf{v}' + c_0, \tag{16}$$

where $c_0 \in \mathbb{R}$ denotes a scalar.

The discretization of the self-similar constraints defined in Eq. 13, implies the discretization of the second order structure function defined in Eq. 10. The integral over directions θ yields a sum on 8 directions: 4 horizontal-vertical directions $\mathbf{n}_h = \{(-1,0),(1,0)\}$ and $\mathbf{n}_v = \{(0,1),(0,-1))\}$ and 4 diagonal directions $\sqrt{2}\mathbf{n}_d = \{(1,1),(1,-1),(-1,-1),(-1,1)\}$ of the bidimensional plane. The continuous motion field discretization yields to rewrite the integral over the spatial domain Ω with a sum over the pixel grid $\boldsymbol{S}$. On this regular grid, the longitudinal velocity increment function is available at scale ℓ either for $\ell \in \mathbb{N}^+$ on horizontal $\mathbf{n}_h$ and vertical $\mathbf{n}_v$ directions, or for $\sqrt{2}\ell \in \mathbb{N}^+$ on diagonal directions $\sqrt{2}\mathbf{n}_d$. To avoid using boundary conditions, we exclude of the sum the grid points $\overline{\mathbf{S}}(\ell)$ which belongs to image borders of width ℓ. A node subset $\mathbf{S}^\ell = \{\mathbf{S} - \{\overline{\mathbf{S}}(\ell)\}$ is thus defined depending on scale. Therefore, at scale ℓ, the discrete second order structure function reads:

$$\mathrm{E}[\delta v_{\parallel}(\ell)^2] = \begin{cases} \frac{1}{4\gamma}\sum_{\mathbf{s}\in\mathbf{S}^\ell}\{\sum_{\mathbf{n}_h}\Big(u(\mathbf{s})-u(\mathbf{s}+\ell\mathbf{n})\Big)^2+\sum_{\mathbf{n}_v}\Big(v(\mathbf{s})-v(\mathbf{s}+\ell\mathbf{n})\Big)^2\}, \text{ if } \ell\in\mathbb{N}^+ \\ \frac{1}{4\gamma}\sum_{\mathbf{s}\in\mathbf{S}^\ell}\sum_{\mathbf{n}_d}\Big(u(\mathbf{s})-u(\mathbf{s}+\ell\mathbf{n})+v(\mathbf{s})-v(\mathbf{s}+\ell\mathbf{n})\Big)^2, \text{ if } \frac{\ell}{\sqrt{2}}\in\mathbb{N}^+ \end{cases} \tag{17}$$

where we have denoted the number of node of the grid $\mathbf{S}^\ell$ by $\gamma = |\mathbf{S}^\ell|$. As detailed in appendix A, the quadratic constraint derivatives can be expressed in the vectorial form $A_\ell\mathbf{v}' - \mathbf{b}_\ell$, where A_ℓ are symmetric positive semi-definite matrices and $\mathbf{b}_\ell$ are vectors of size n. Thus, the constraints read using variables $\mathbf{v}'$:

$$g_\ell(\mathbf{v}) = \frac{1}{2}\mathbf{v}'^T A_\ell \mathbf{v}' - \mathbf{b}_\ell^T\mathbf{v}' + c_\ell = 0, \ \ \forall \ell \in \mathbf{I}, \tag{18}$$

where $c_\ell \in \mathbb{R}$ are scalars. Let us remark that the discretization of the self-similar constraints does not rely on any approximation conversely to standard regularization schemes such as in Horn & Schunck (1981) where continuous spatial derivatives have to be approached by discrete operators. The constraint motion estimation problem defined in Eq. 15 can thus be rewritten in its discrete form as:

$$(P)\begin{cases} \min_{\mathbf{v}} \ f_d(I,\mathbf{v}) = \frac{1}{2}\mathbf{v}'^T A_0\mathbf{v}' - \mathbf{b}_0^T\mathbf{v}' + c_0. \\ \text{subject to:} \\ g_\ell(\mathbf{v}) = \frac{1}{2}\mathbf{v}'^T A_\ell\mathbf{v}' - \mathbf{b}_\ell^T\mathbf{v}' + c_\ell = 0, \ \ \forall \ell \in \mathbf{I} \\ \mathbf{v} = \mathbf{v}' + \tilde{\mathbf{v}} \in \mathbb{R}^n. \end{cases} \tag{19}$$

3.4 Dual problem and optimal solution

To define optimality conditions, the lagrangian function $L(\mathbf{v}, \boldsymbol{\lambda})$ associated to (P) is introduced:

$$L(\mathbf{v}, \boldsymbol{\lambda}) = f_d(I, \mathbf{v}) + \sum_{\ell} \lambda_\ell g_\ell(\mathbf{v}), \;\; \boldsymbol{\lambda} = \{\lambda_\ell\}. \tag{20}$$

In the lagrangian duality formalism, the optimal solutions of the so-called *primal* problem P, are obtained by searching *saddle points* of the lagrangian function. *Saddle points* denoted by $(\mathbf{v}^*, \boldsymbol{\lambda}^*)$ are defined as the solutions of the so-called *dual* problem:

$$(D) \left\{ \begin{array}{l} L(\mathbf{v}^*,\boldsymbol{\lambda}^*) = \max_{\boldsymbol{\lambda}} w(\boldsymbol{\lambda}) = \max_{\boldsymbol{\lambda}} \{\min_{\mathbf{v}} L(\mathbf{v}, \boldsymbol{\lambda})\} \\ \lambda_\ell \in \mathbb{R}, \;\; \forall \ell \in \mathbf{I} \end{array} \right. , \tag{21}$$

where $w(\boldsymbol{\lambda})$ denotes the *dual* function. As the functions f and g_ℓ are convex and as the constrained group is not empty, for positive lagrangian multipliers λ_ℓ, L is convex and the minimization problem (P) has a unique *saddle point i.e.* an optimal solution $\mathbf{v}^*$ which is unique. More details for such convex functionals and the convergence of the related minimization problems can be found in Weickert & Schnörr (2004). Lagrangian multipliers $\{\lambda_\ell\}$, which represent the regularization parameters at scales $\{\ell\}$, are then optimally given by the coordinates of the saddle point. Note that for negative lagrangian multipliers, the convexity of the functional is no longer insured, and there is no guarantee of the solution unicity. Nevertherless, there exists local optimal solutions.

3.5 Convex optimization

The minimum $\hat{\mathbf{v}}'$ of a locally convex lagrangian function at point $\boldsymbol{\lambda}$ can be obtained by cancelling the gradient:

$$\nabla_{\mathbf{v}} L(\mathbf{v}, \boldsymbol{\lambda}) = \nabla_{\mathbf{v}} f_d(I, \mathbf{v}) + \sum_{\ell} \lambda_\ell \nabla_{\mathbf{v}} g_\ell(\mathbf{v}) = 0, \tag{22}$$

which reduces (using Eq. 16 and Eq. 18) to solve the large linear system:

$$(A_0 + A)\hat{\mathbf{v}}' = \mathbf{b}_0 + \mathbf{b}, \tag{23}$$

with $A = \left(\sum_\ell \lambda_\ell A_\ell \right)$ and $\mathbf{b} = \sum_\ell \lambda_\ell \mathbf{b}_\ell$. In appendix A, we show that the linear system components A_ℓ and $\mathbf{b}_\ell$ are constituted by the superposition of a collection of discrete operators obtained in a centered 2-nd order finite difference scheme on a grid of mesh ℓ, which corresponds to 2-nd order derivatives at

different scales. Since we have no guarantee that matrix $A_0 + A$ is positive-definite depending on the sign of lagrangian multipliers λ_ℓ, the resolution of the large system of Eq. 23 is efficiently achieved using a Conjugate Gradient Squared (CGS) method with an incomplete LU preconditionner. The dual function is then given by:

$$w(\boldsymbol{\lambda}) = \frac{1}{2}\hat{\mathbf{v}}'^T\Big(A_0 + A\Big)\hat{\mathbf{v}}' - \Big(\mathbf{b}_0 + \mathbf{b}\Big)^T\hat{\mathbf{v}}' + c_0 + c, \tag{24}$$

where the constant $c = \sum_\ell \lambda_\ell c_\ell$. The dual function is by definition concave and possesses so-called *sub-gradients* equal to $g_\ell(\hat{\mathbf{v}}' + \tilde{\mathbf{v}})$. We employ a classical gradient method to find $\boldsymbol{\lambda}^*$ which maximizes the dual function and thus obtain the solution $\mathbf{v}^*$. Finally, the constrained motion estimation method results in a *Uzawa* algorithm, which is used to converge towards the saddle point $(\mathbf{v}^*, \boldsymbol{\lambda}^*)$, *i.e.* the optimal motion estimate under self-similar constraints. To cope with non-linearity of the data term, incremental motion fields are estimated using motion compensated images and a multiresolution data representation[3]. An important remark is that once the regularization coefficient vector $\boldsymbol{\lambda}^*$ has been estimated for two consecutive images of the sequence, assuming motion stationarity, only one step of the *Uzawa* algorithm is needed to process the following image pairs. Therefore, the complexity of the algorithm reduces to the resolution of the linear system by CGS, that is $\mathcal{O}(\kappa n)$, where κ is the conditioning number of $A_0 + A$. The multiresolution Uzawa algorithm is presented below.

[3]Note that the scaling law factor β must be scaled by the multiplicative factor $(2^j)^{-\zeta+2}$ at each scale j of the multiresolution pyramid.

- Iterate until resolution j reaches the finest level:
  - Compensate image $I_{(j)}$ with coarse motion estimate $\tilde{\mathbf{v}}_{(j)}$
  - Iterate until convergence from initial point $(\tilde{\mathbf{v}}_{(j)}, \boldsymbol{\lambda}^0_{(j)})$ with $\boldsymbol{\lambda}^0_{(j)} > 0$:
    - At iteration k, find increment $\hat{\mathbf{v}}'_{(j)}$ by solving Eq. 23
    - Define $\boldsymbol{\lambda}^{k+1}_{(j)}$ by a gradient ascent step:

$$\forall \ell \in \mathbf{I},\ \lambda^{k+1}_{\ell,(j)} = \lambda^k_{\ell,(j)} + \rho^k g_\ell(\hat{\mathbf{v}}'_{(j)} + \tilde{\mathbf{v}}_{(j)})$$

  - $(\mathbf{v}^*_{(j)}, \boldsymbol{\lambda}^*_{(j)}) = (\hat{\mathbf{v}}'_{(j)} + \tilde{\mathbf{v}}_{(j)}, \boldsymbol{\lambda}^k_{(j)})$
  - Define $\tilde{\mathbf{v}}_{(j-1)}$ by projection of $\mathbf{v}^*_{(j)}$ on level $j-1$
  - $j = j - 1$

ρ^k denotes the step size at iteration k. This latter parameter is relaxed at each iteration (Held *et al.*, 1974).

Multiresolution Uzawa algorithm converging towards saddle point $(\mathbf{v}^*, \boldsymbol{\lambda}^*)$**.**

4 Selection of a multiscale prior model

In the previous section, we have proposed to model motion in images conditioned by a prior scaling law model (defined by power law factor β and exponent ζ or slope in log-log coordinates). We now want to select the most appropriate scaling law model for motion estimation given only the image data. Model selection will yield several advantages:

- first, prior model inference will result in a non-parametric method (*i.e.* without any explicit smoothing parameter),
- second, modeling will allow us to cope with uncertainties in turbulence theoretical predictions associated, *e.g.*, to intermittency effects,
- third, inference of (β, ζ) will enable us to reveal important physical quantities in turbulence such as power law exponents (linked to motion regularity), flux across scales, or the energy and enstrophy dissipation rates.

After reformulating the constrained motion estimation problem in a probabilistic framework, we show how the multiscale prior model likelihood probability given the image data can be evaluated.

4.1 Bayesian hierarchical modeling

Bayes' rule provides a nice framework to evaluate this model likelihood probability, the so called *evidence*. Indeed, a probabilistic reformulation of the global motion estimation problem yields a 3-level hierarchical model linking image, motion and scaling laws:

$$I \rightarrow \mathbf{v} \rightarrow \beta, \zeta \tag{25}$$

Note that regularization weights $\boldsymbol{\lambda}^*(\zeta, \beta)$ do not appear in the variable hierarchy as they are deterministically given for fixed (ζ, β). Applying Bayes' rule, we obtain two levels of inference in this hierarchy (MacKay, 1992):

- *Scaling model fitting.* We assume some scaling model parameters (ζ, β), i.e regularization weights $\boldsymbol{\lambda}^*(\zeta, \beta)$ (lagrangian multipliers) provided by the dual formalism. Solving the primal problem in the previous section is equivalent to infer a velocity field $\mathbf{v}^*$ according to a *Maximum A Posteriori* (MAP) criterion. The *posterior* PDF of this first level of inference is given by Bayes' relation:

$$p(\mathbf{v}|I,\zeta,\beta) = \frac{p(I|\mathbf{v},\zeta,\beta)p(\mathbf{v}|\zeta,\beta)}{p(I|\zeta,\beta)} = \frac{\text{likelihood} \times \text{prior}}{\text{evidence}}$$

$$\propto p(I|\mathbf{v},\zeta,\beta)p(\mathbf{v}|\zeta,\beta) \tag{26}$$

  and is a Gibbs PDF which reads

$$p(\mathbf{v}|I,\zeta,\beta) = \frac{\exp\{-\frac{1}{2}\mathbf{v}'^T(A_0 + A(\zeta,\beta))\mathbf{v}' + (\mathbf{b}_0 + \mathbf{b}(\zeta,\beta))^T\mathbf{v}' - c_0 - c(\zeta,\beta)\}}{Z_L(\zeta,\beta)} \tag{27}$$

  where $Z_L(\zeta, \beta)$ denotes the normalization constant also called the partition function.

- *Scaling model selection.* A second level of inference can be performed on the scaling law model parameters (ζ, β) using Bayes' relation:

$$p(\zeta, \beta|, I) = \frac{p(I|\zeta, \beta)p(\zeta, \beta)}{p(I)} \propto p(I|\zeta, \beta)p(\zeta, \beta). \tag{28}$$

For a flat prior on variables (ζ, β), the MAP of Eq. 28 w.r.t self-similar model parameters (ζ, β) is simply the *Maximum Likelihood* (ML) estimate or in other words the maximum of the *evidence* $p(I|\zeta, \beta)$. The *evidence* can be obtained by marginalization w.r.t. the velocity field:

$$p(I|\zeta, \beta) = \int_{\mathbb{R}^n} p(I|\mathbf{v}, \zeta, \beta)p(\mathbf{v}|\zeta, \beta)\mathrm{d}\mathbf{v}. \tag{29}$$

Direct calculation of this integral is impractical due to its huge dimension. However, let us recall that the *evidence* is the normalization constant (w.r.t. velocity field $\mathbf{v}$) which has been ignored in the first level of inference (Eq. 26). Therefore, we can rewrite the *evidence* as a normalization constant ratio:

$$p(I|\zeta, \beta) = \frac{\text{likelihood} \times \text{prior}}{\text{posterior}} = \frac{Z_L(\zeta, \beta)}{Z_{f_d} Z_{g_\ell}(\zeta, \beta)}, \tag{30}$$

where Z_{f_d} and Z_{g_ℓ} denote the normalization constants associated to the *likelihood* and the Gibbs *prior* PDF.

4.2 Scaling model selection by evidence

The scaling law model evidence can now be evaluated as a normalization constant ratio. First, the *likelihood* PDF $p(I|\mathbf{v}, \zeta, \beta)$ related to a quadratic optic-flow data term f_d is a normalized m dimensional gaussian with uncorrelated components. Thus its normalization constant reads:

$$Z_{f_d} = \int_{\mathbb{R}^m} \exp\{-f_d(I, \mathbf{v})\}\mathrm{d}I = (2\pi)^{m/2}, \tag{31}$$

where m denotes the number of pixels. Therefore Z_{f_d} is a constant w.r.t. (ζ, β) which can be ignored. Then, the normalization constant integral Z_L of the *posterior* PDF of Eq. 27 can be calculated using

Laplace's approximation (see for example MacKay (2003)) :

$$\begin{aligned} Z_L(\zeta,\beta) &= \int_{\mathbb{R}^n} \exp\{-L(\mathbf{v},\boldsymbol{\lambda}^*(\zeta,\beta))\}\mathrm{d}\mathbf{v} \\ &\simeq \exp^{\{-L(\mathbf{v}^*(\zeta,\beta),\boldsymbol{\lambda}^*(\zeta,\beta))\}} 2\pi^{\frac{n}{2}} \det(A_0+A(\zeta,\beta))^{-\frac{1}{2}}, \end{aligned} \tag{32}$$

where we recall that $\mathbf{v}^*$ is the MAP estimate, $\boldsymbol{\lambda}^*$ is the associated set of lagrangian multipliers and where $n = 2m$ denotes the number of unknown velocity variables. For gaussian distributions, the Laplace equality is exact and for other distributions it still constitutes a good approximation (Gull, 1989). The determinant of such large and sparse matrices can be efficiently approximated via an incomplete LU decomposition. Finally, the *prior* PDF can be written as:

$$p(\mathbf{v}|\zeta,\beta) = \frac{\exp^{\{-\frac{1}{2}\mathbf{v}'^T A(\zeta,\beta)\mathbf{v}'+\mathbf{b}^T(\zeta,\beta)\mathbf{v}'-c(\zeta,\beta)\}}}{Z_{g_\ell}(\zeta,\beta)}. \tag{33}$$

This self-similar *prior* is degenerated and has an infinity set of maxima corresponding to the infinite set of admissible velocity field solutions respecting the self-similar constraint. To make this prior well-defined, we use dirichlet boundary conditions (only for evaluating the evidence). Note that the precise value on the boundaries does not need to be specified since it modifies the vector $\mathbf{b}$ but does not have impact on the hessian matrix A (even if the form of A is changed considering boundary conditions). Considering these boundaries, we get a slightly changed hessian matrix A which is of full rank. As previously, the normalization constant can be calculated using a gaussian approximation:

$$\begin{aligned} Z_{g_\ell}(\zeta,\beta) &= \int_{\mathbb{R}^n} \exp\{-\sum_\ell \lambda_\ell^*(\zeta,\beta) g_\ell(\mathbf{v})\}\mathrm{d}\mathbf{v} \\ &= \underbrace{\max_{\mathbf{v}}\Big(\exp^{\{-\sum_\ell \lambda_\ell^*(\zeta,\beta)g_\ell(\mathbf{v})\}}\Big)}_{=1} 2\pi^{\frac{n}{2}} \det A(\zeta,\beta)^{-\frac{1}{2}} \end{aligned} \tag{34}$$

As the set of admissible solution for $\mathbf{v}$ for the self-similar constraint is not empty, the exponential term in Eq. 34 has a maximum value equal to 1. Finally, using Eq. 30, Eq. 32 and Eq. 34, the log evidence of the scaling model reads:

$$\log p(I|\zeta,\beta) \propto \underbrace{-f_d(\mathbf{v}^*,I)}_{\text{data term}} \underbrace{-\frac{1}{2}(\log\frac{\det(A_0+A)}{\det(A)})}_{\text{log Occam factor}} \tag{35}$$

where for simplification we have dropped the dependance to parameters (ζ, β). The last terms, known as *Occam factor* (Jaynes, 2003; MacKay, 2003), penalizes the model complexity. It is the ratio of the posterior accessible volume on the prior accessible volume in $\mathbf{v}$ (a variance ratio in 1D). Note that the term $\sum_\ell \lambda_\ell^* g_\ell(\mathbf{v}^*)$ does not appear in Eq. 35 as the constraints vanish at the saddle point.

5 Experiments

5.1 Simulated bidimensional turbulence

To evaluate the performance of the self-similar regularization, a synthetic particle image sequence was generated based on forced two-dimensional turbulence obtained by direct numerical simulation (DNS) of Navier-Stokes equations with a Reynolds number of 3000, and a particle image generator (Carlier & Wieneke, 2005). Figure 2 presents one of the particle images of 256×256 pixels and a scalar representation of the true underlying velocity field displayed in figure 1. In these visualizations color and intensity code vector orientations and magnitudes (Baker *et al.*, 2007). The motion estimate minimizing the quadratic linearized OFC based data-term (Eq. 8) under self-similarity constraints is displayed for comparison in figure 2. Details of this estimation are discussed below.

5.1.1 Evaluation of model selection

The evidence of the self-similar model in the scale range of $\mathbf{I} = [1, 10]$ pixels (corresponding either to dissipation or the enstrophy cascade) is evaluated by sampling ζ respectively around the theoretical value of 2 for the power law exponent, and by sampling factor β around a Least Square (LS) estimate given by any rough estimator (*e.g.* Horn & Schunck (1981)). Figure 3 shows the behavior of the log-evidence and the Root Mean Square Error (RMSE) w.r.t the scaling law slope and factor. Note that the evidence reaches its maximum in $\zeta = 1.90$ and $\beta = 0.0026$ which corresponds to the RMSE minimum but not to the exponent fitting ground truth ($\zeta = 1.94$ in the LS sense). As RMSE and minus the logarithm of the evidence seem to define parabolas around their minimum, we fit them with quadratic functions for visualization convenience. While parabolas share roughly the same minimum in β, it can be noted a slight shift of 0.018 between the two parabolas in ζ. This shift has however a reasonable incidence

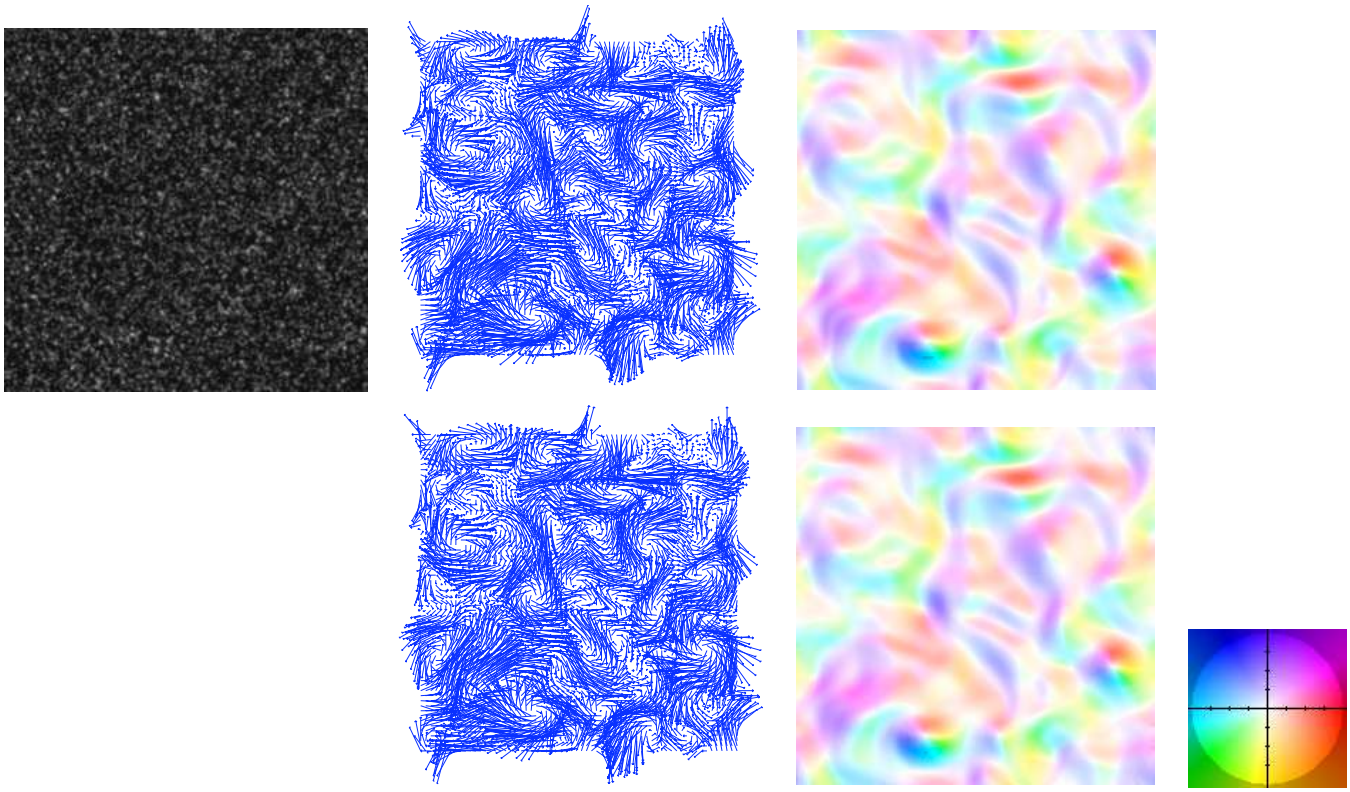

Figure 2: ***Bidimensional turbulence. Above.*** *Particle image at initial time (left). True velocity field (middle) and its scalar (right) representation.* ***Bellow****. Estimated velocity field (middle) and its scalar (right) representation together with (Baker* et al.*, 2007) color system for scalar visualization of vector fields.*

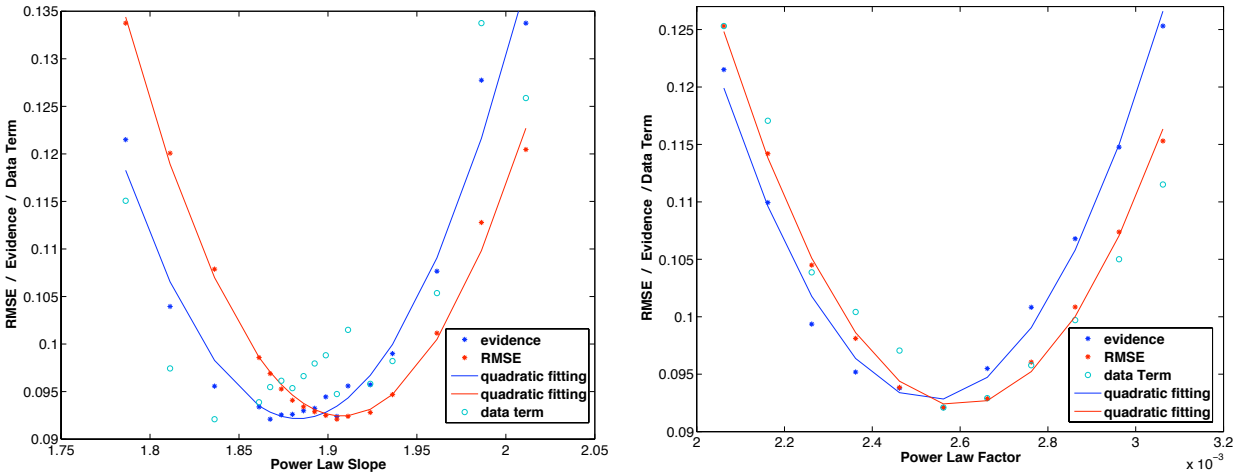

Figure 3: ***Scaling model selection.*** *Behavior of data term and minus the evidence logarithm w.r.t slope ζ (**left**) and factor β (**right**) in comparison to the RMSE. For comparison, evidence and data term ranges of value have been rescaled on the RMSE.*

in the error increase. The power law minimizing the evidence probability is plotted in figure 5 together with the true second order structure function $\mathrm{E}[\delta v_{\|}(\ell)^2]$. Obviously, the most evident scaling model will not necessarily correspond to a minimum in the RMSE or to the slope fitting the best the ground truth data in a LS sense. Nevertheless, it constitutes a theoretical sound and reliable criteria for selecting the scaling model. In particular, as shown in figure 3 it is much more efficient than the data-term error. The variations of the normalized increments PDF accross scales produced either by the DNS (see figure 1) or by the proposed motion estimator (see figure 4) can hardly be distinguished. It proves that the flow is in this case strictly self-similar to a good approximation. In order to verify that we obtained converged statistics for evaluation of the structure functions, as suggested in Gotoh *et al.* (2002), we examine the convergence towards a flat curve of the accumulated moments :

$$C_p(z,\ell) = \int_0^z |\delta v_{\|}(\ell)'|^p p'(\delta v_{\|}(\ell)') d\delta v_{\|}(\ell)', \tag{36}$$

where $p'(\delta v_{\|}(\ell)') = \sigma_\ell p_\ell(\delta v_{\|}(\ell)/\sigma_\ell)$ is the PDF of the normalized increments $\delta v_{\|}(\ell)' = \delta v_{\|}(\ell)/\sigma_\ell$ with σ_ℓ denoting the standard deviation. It is clearly visible in figure 4 that $C_2(z,\ell)$ tends to be flat for normalized increments greater than 3. As this normalized value does not belong to the tail of the PDF,

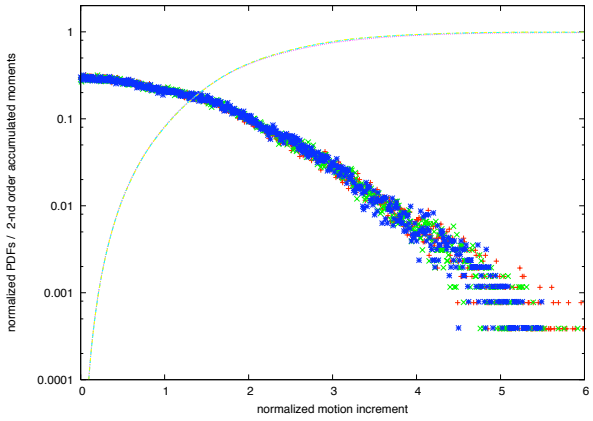

Figure 4: ***Auto-similarity hypothesis & convergence of 2-nd order statistics***. *Similarity through scales of estimated normalized increments PDFs* $\sigma_\ell p_\ell(\frac{\delta v_{\|}(\ell)}{\sigma_\ell})$ *and 2-nd order accumulated moments* $C_2(z,\ell)$ *for* $\ell = 1, 2, 4$ *respectively displayed in red, green and blue.*

one can say that the second order statistics used for motion estimation and model selection are converged.

5.1.2 Evaluation of motion estimation

A comparison of end point errors (L^1 norm of velocity vector difference) and Barron's angular errors (Barron *et al.*, 1994) with state of the art estimators is presented in figure 6. Based on these criteria, the proposed method outperforms in average most accurate operational correlation-based techniques[4], first order (Horn & Schunck, 1981) and div-curl (Corpetti *et al.*, 2002; Yuan *et al.*, 2007) regularizers. Let us remark that for this incompressible bidimensional experiment, we have subtracted the divergent component of the estimated flow using Helmoltz decomposition in order to make results comparable to (Yuan *et al.*, 2007). The error maps comparison displayed in the same figure shows that the proposed regularization enhances in particular the estimation of small scale displacements compared to other approaches. At larger scales, the method also outperforms other approaches. Nevertheless, medium sized structures very similar to those obtained in (Yuan *et al.*, 2007) can be observed. In figure 5, the 2-nd order structure function log plots show that, especially in the scale interval where constraints have been applied, the estimation fits perfectly the ground truth. The power law maximizing the model evidence fits in this

[4]Operational PIV correlation-based software from *LaVision* company (*www.lavision.de*) gave a RMSE of 0.1313

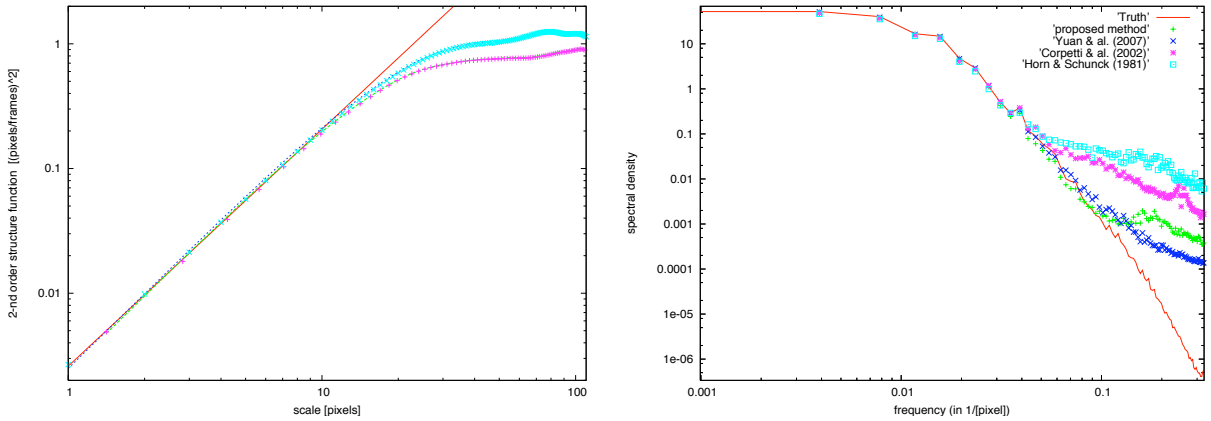

Figure 5: ***2-nd order statistics. Left*** *: Power law maximizing evidence (continuous red line). True (dash line) and estimated (crosses) 2-nd order structure functions in horizontal-vertical (in blue and turquoise) and diagonal (in pink and green) directions .* ***Right*** *: Energy spectra $E(k)$ of first order (in turquoise), div-curl (in blue or pink) and self-similar (in green) regularizers compared to the true (in red) spectrum.*

interval also very well the ground truth. It is observed that the turbulent flow possess isotropic statistics at small scales since structure functions calculated in horizontal-vertical and in diagonal directions are nearly identical. We also compute the average L_2 norm of the fourier transform over each line of the horizontal velocity component as it produces a 1D energy spectrum $E(k)$ representation which enables to analyze motion at the different scales. The log plot of the ground truth energy spectrum exhibits in figure 5 a slope close to -5 which is much steeper than the -3 slope expected according to *Kraichnan*'s theory, but which is not unusual for DNS of bidimensional turbulence. Unfortunately, for slopes outside the interval $]-1,-3[$, no correspondence can be made with the slope of the related 2-nd order structure function (Frisch, 1995). This explains that, although the power law of the 2-nd order structure function has been accurately estimated, the tail of the estimated spectrum is not constrained to fit to the ground truth -5 slope. Nevertheless, the proposed regularization restitutes the spectrum at higher frequencies than other regularizers.

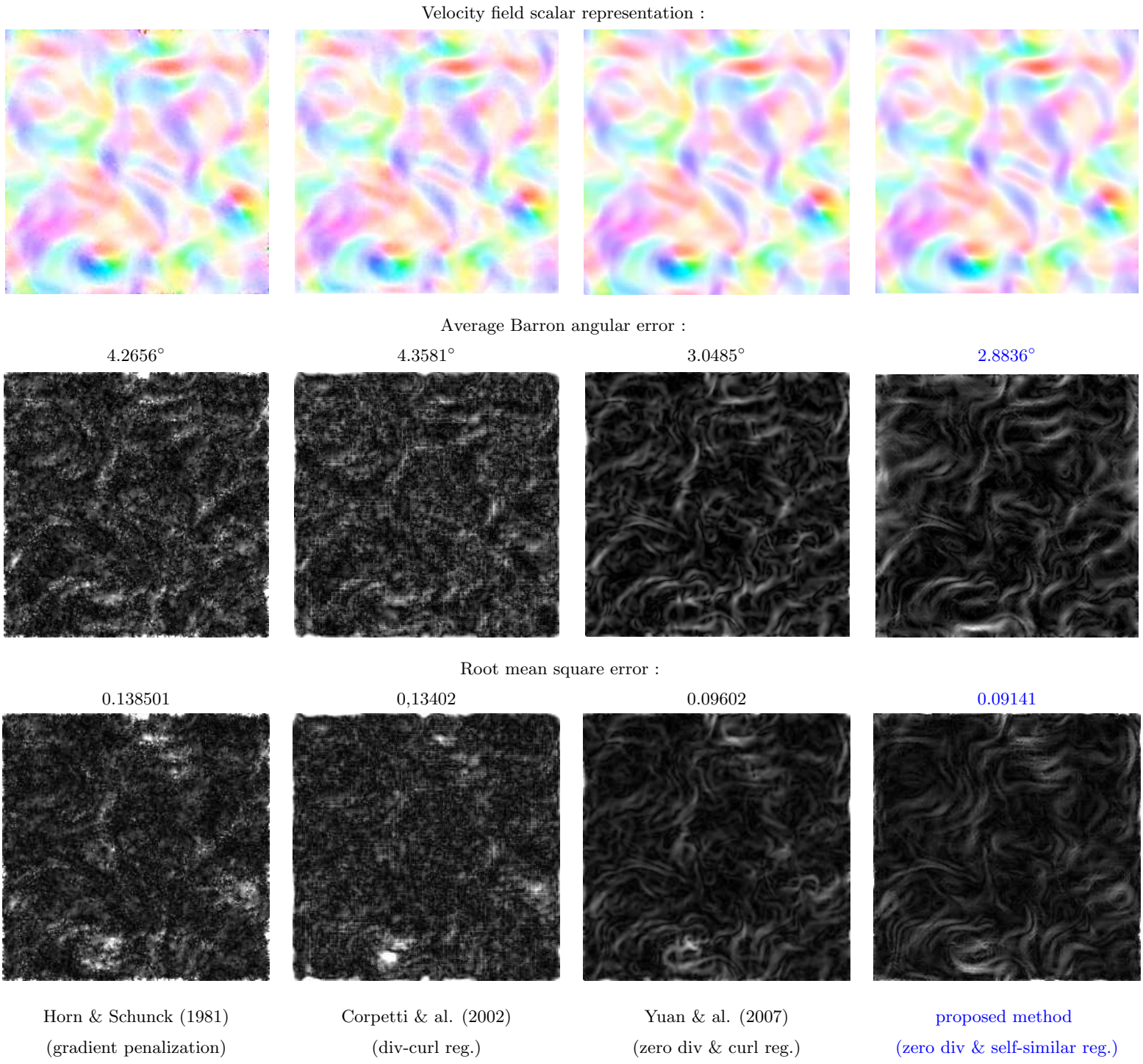

Figure 6: ***Motion estimation accuracy.*** *Velocity field scalar representation (1-st line), Barron's angular error (2-nd line) and end point errors (3-rd line) comparisons with state of the art. RMSE and average Barron angular error are displayed above the figures.*

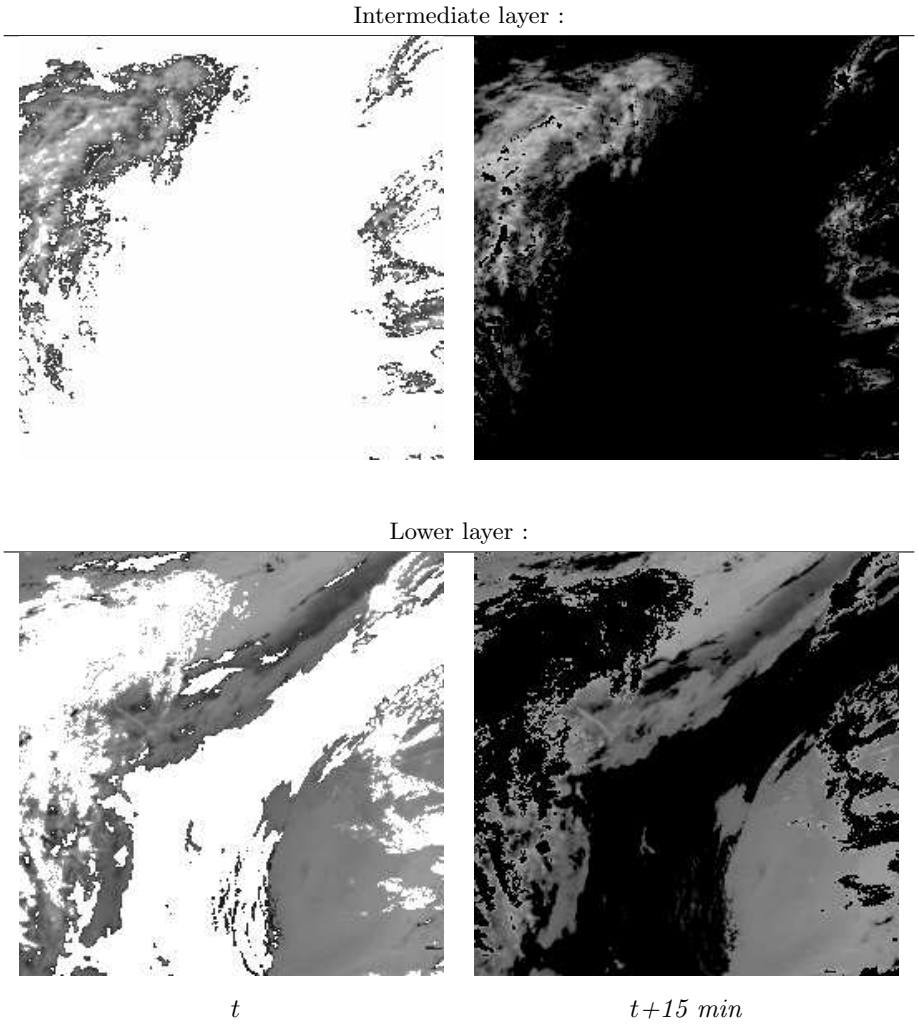

Figure 7: ***Input meteorological images.*** *Sparse pressure difference maps of layers at intermediate (above) and low (below) altitude. White pixels of image at time* t *and black pixels at time* $t + 15$ *minutes are areas with no observations. The images characterize the layers evolution in a time interval of 15 minutes.*

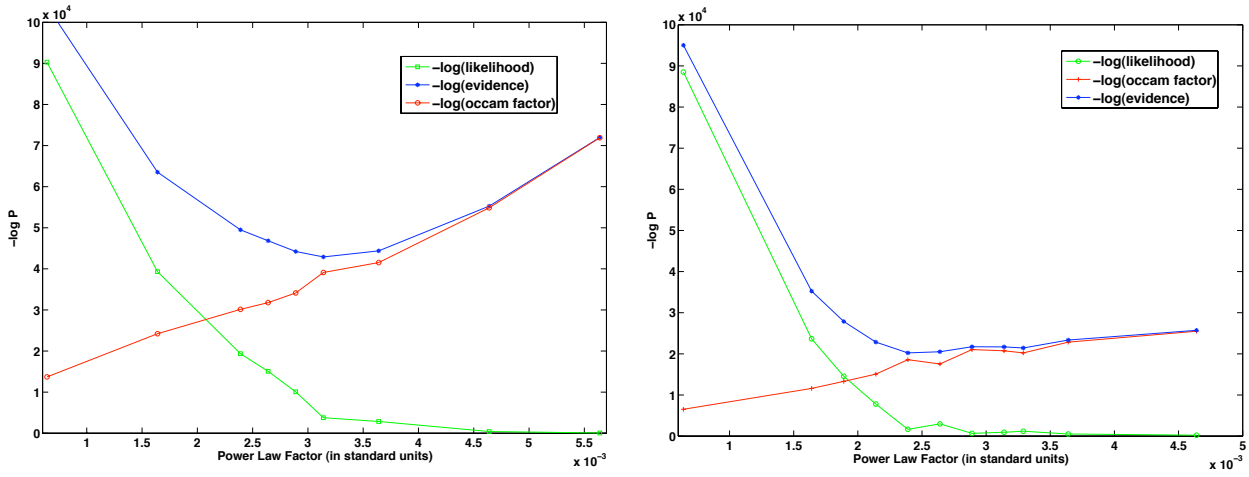

Figure 8: ***Evidence maximization w.r.t energy flux.*** *Minus log of evidence (blue), likelihood (green) and Occam factor (red) v.s. power law factor β (i.e. energy flux ϵ) for horizontal winds at low (**left**) and at intermediate (**right**) altitude*

5.2 Atmospheric turbulence

The multi-scale regularizer has then been assessed on real data. A benchmark constituted with METEOSAT Second Generation meteorological image sequences acquired above the north Atlantic Ocean at a rate of an image every 15 min has been used. The image spatial resolution is 3×3 km^2 at the center of the whole Earth image disk. According to the physical-based methodology proposed in (Heas *et al.*, 2007; Corpetti *et al.*, 2008), a set of sparse pressure difference images of 256×256 pixels related to a stack of layers (low and intermediate altitude) have been derived. As detailed in appendix B, pressure-based cloud classification and images of top of cloud pressure have been used to create the set of input images displayed in figure 7. We then used the direct observation model designed by the authors for those sparse images, which is detailed in appendix B. It is based on layer mass conservation which relates the image intensity functions to vertically averaged horizontal wind fields.

5.2.1 Power law characterization

Direct energy flux by evidence maximization. In this section, we assume that the exponent $\zeta = 2/3$ predicted by *Lindborg* in the direct energy cascade holds in the range $\mathbf{I} = [1, 4]$ pixels equivalent to $\mathbf{I} =$

[3, 12] km (the direct energy cascade is only visible for the 2-nd order structure function up to separation of about 10 kilometers (Lindborg, 1999)). We thus only need to infer the parameter β by evidence maximization. Figure 9 shows that the evidence maximum is around $\hat{\beta}_{mid} = 0.0024$ for the middle layer and around $\hat{\beta}_{low} = 0.0031$ for the lower layer. This plot also illustrates the shared contribution of the *Occam* factor and the data term in the evidence. Note that alone, the data term is an insufficient criteria for model selection as it vanishes almost completely for large values of β. The model proposed in (Lindborg, 1999) provides an expression for the 2-nd order structure function and the energy spectrum:

$$\begin{cases} \mathrm{E}[\delta v(\ell)^2] = C_2 \epsilon^{\frac{2}{3}} \ell^{\frac{2}{3}} + b\,\ell^2 - c\,\ell^2 \log \ell, \\ E(k) = C_2 \epsilon^{\frac{2}{3}} k^{-\frac{5}{3}} + c\,k^{-3}/2. \end{cases} \tag{37}$$

In Eq. 37, the energy flux can be related in the scale range **I** to the power law factor by $\beta = C_2 \epsilon^{\frac{2}{3}}$. In the previous equations, b and c denote parameters and $C_2 \simeq 6$ is a Kolmogorov constant. Therefore, the maximum of the evidence also provides the most likely energy flux ϵ (also equal to the energy dissipation rate):

$$\begin{cases} \hat{\epsilon}^{mid} \simeq 0.79 \times 10^{-5} m^2 s^{-3} \\ \hat{\epsilon} low \simeq 1.20 \times 10^{-5} m^2 s^{-3}. \end{cases} \tag{38}$$

These estimates have the same order of magnitude as previous reported results based on aircraft data analysis[5]. Thus this agreement is in our opinion very good as the measure is only based on image data. An energy spectrum comparison in figure 9 shows that on the contrary to the motion estimator proposed in Heas *et al.* (2007), the present method does not underestimate the energy flux. It should be noted that in the proposed estimation approach, as the evidence maximization does not depend on motion variables, energy flux is obtained directly from the image intensity function conversely to other approach which need to first extract pseudo motion observations from the images and then estimate independently self-similar parameters using for example wavelet-based estimation methods (Flandrin, 1992; Abry *et al.*, 1995). Concerning the direction of the energy cascade, the third order structure function of the lower layer motion displayed in figure 9 shows a direct cascade with a linear dependance of $-\hat{\epsilon}^{low}\ell$ in the scale range $[20, 50]$ km. However, the direct cascade is not visible for the intermediate layer motion. Besides the fact that three dimensional behaviours (direct energy cascades) are more likely to occur in the boundary layer than at higher altitude, another explanation of the absence of the direct cascade at intermediate altitude can be given by examining the convergence of the third order accumulated moments.

[5] Lindborg & Cho (2001) estimated an average energy flux value of $\epsilon \sim 6 \times 10^{-5} m^3 s^{-3}$ for the stratosphere. A collection of other *in situ* measurements shows a typical value close to $\sim 10^{-5} m^3 s^{-3}$ (Dewan, 1997)

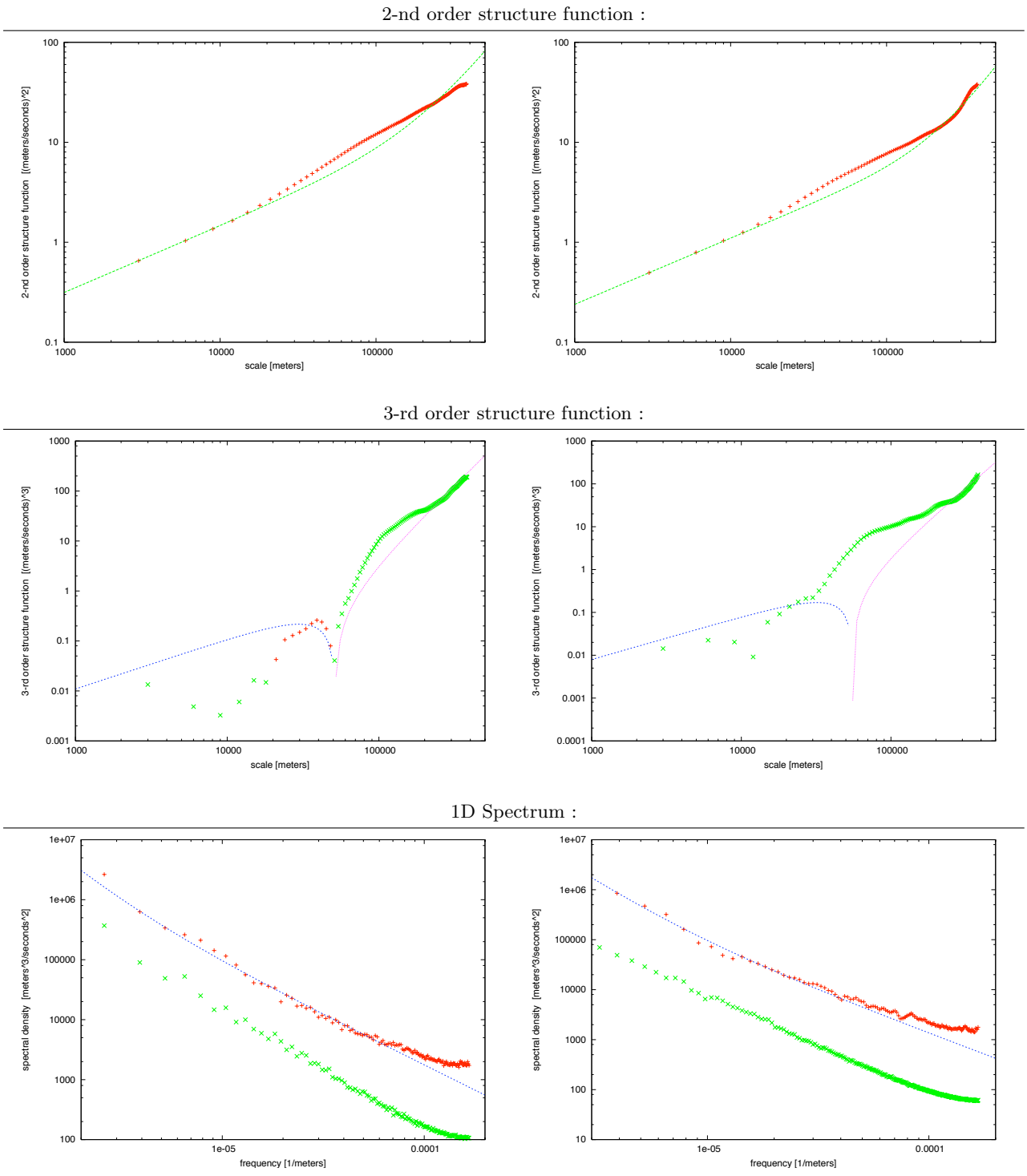

Figure 9: ***Energy spectra (line below), 2-nd (line above) and 3-rd (middle line) order structure functions at low (left column) and intermediate (right column) altitudes***. *2-nd order structure functions (red crosses) are plotted with their associate models (green dashed line). 1D energy spectra obtained by our approach (red crosses) can be compared to their models (blue dashed line) and to results from Heas* et al. *(2007) (green stars). 3-rd order structure functions (plotted in green for positive values and in red for negative values) can be compared to their associate models (pink dashed line for positive values and blue dashed line for negative values).*

Moments convergence. In order to check the convergence of the second and third order structure functions, we examine if the accumulated moments have converged towards flat curves when the unlikely events occur (tail of PDF). In figure 10, curves $C_2(z,\ell)$ and $C_3(z,\ell)$ show that second and third order moments are reasonably converged. However, we observe that accumulated moments show a faster convergence for the lower layer motion. This obviously results from the degree of sparseness of the image data which increases with altitude. Furthermore, curves show that the third order moments are better converged at large scales ($\ell \gtrsim$50 km) than at small scales ($\ell \lesssim$50 km). In fact, the normalized motion increment PDFs show more significant deviations from self-similarity as the scale studied is decreased. This is illustrated by the development in the PDF of strong tails that depart more and more from Gaussian behavior, and is the result of intermittency: turbulence comes in gusts, and scarce regions with strong gradients develop in the flow as the result of nonlinearities. The development of these strong events also make the convergence of high order moments slower, as more data is needed to have enough statistics to resolve the small scale events.

Direct enstrophy flux by least square fitting. A least square estimate of the enstrophy flux $\hat{\epsilon}_\omega$ transmitted at large scales can be obtained by fitting w.r.t. $\hat{\epsilon}_\omega$ the third order structure function to its model given by Eq. 11 in the converged scale range ($\ell > 50$ km). In particular, at the upper range of the cascade, positive cubic power laws can clearly be noticed for both layers. The least square average enstrophy flux estimates are:

$$\begin{cases} \hat{\epsilon}_\omega^{mid} \simeq 2.58 \pm 0.78 \times 10^{-15} s^{-3} \\ \hat{\epsilon}_\omega^{low} \simeq 4.16 \pm 0.23 \times 10^{-15} s^{-3} \end{cases} \tag{39}$$

These results are also consistent with previous published results[6]. Third order structure function models obtained by LS estimation are displayed in figure 9. Second order structure function and energy spectrum models given by Eq. 37 can also be adjusted in a LS sense. Parameters b and c can be estimated for scales $\ell > 50$ km. Figure 9 shows the 2-nd order structure functions and energy spectra together with their associate models.

[6] These value agree well with an early estimate of $\sim 10^{-15} s^{-3}$ obtained by Charney (1971). They are also consistent with a more recent estimation of Cho & Lindborg (2001) of the average enstrophy flux observed in the stratosphere. Tung (2003) then obtained this same result by simulation.

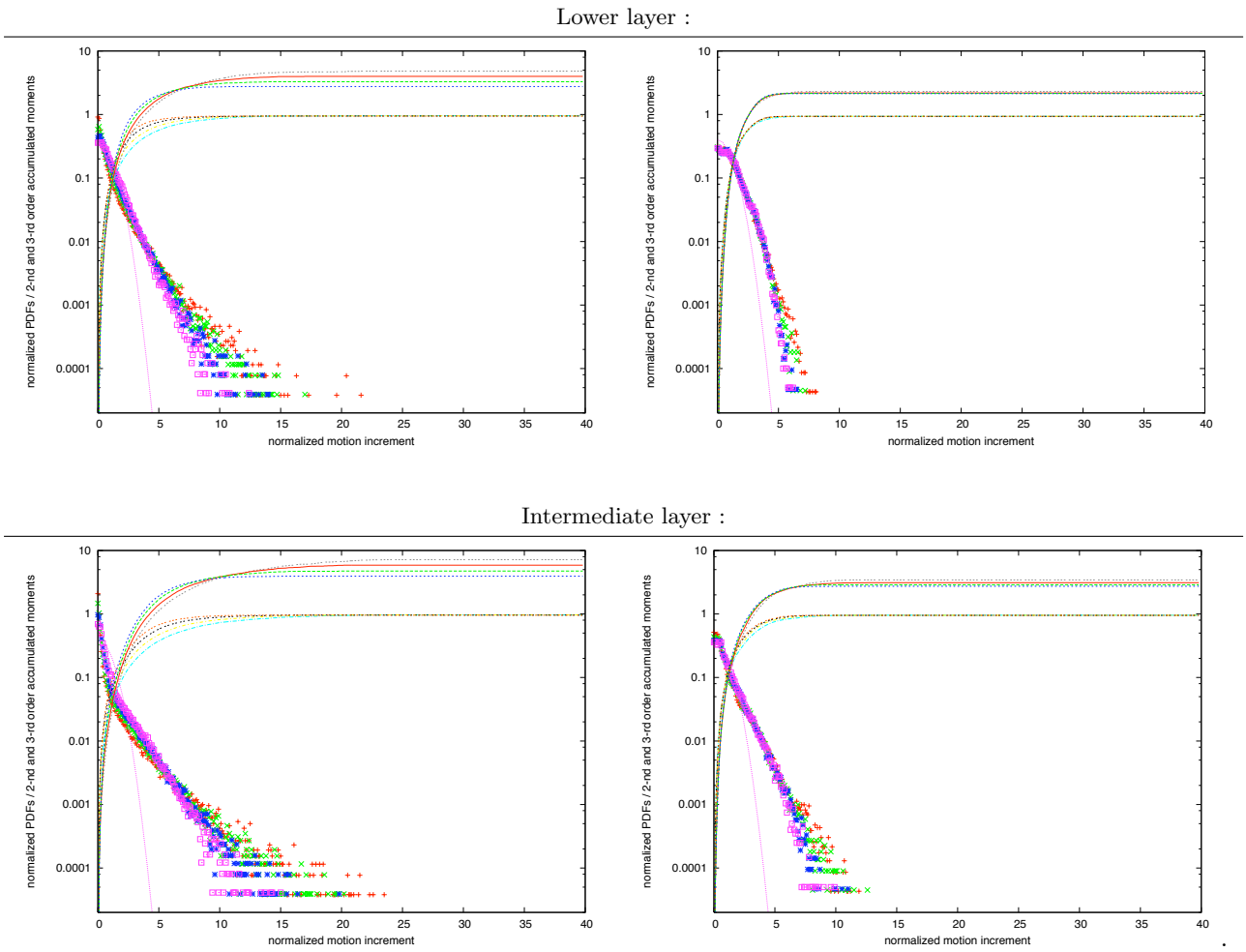

Figure 10: ***Self-similarity and statistics convergence.*** *Similarity through scales of normalized increment PDFs* $\sigma_\ell p_\ell(\delta v_\parallel(\ell)/\sigma_\ell)$ *and 2-nd / 3-rd order accumulated moments for winds at low and intermediate altitude.* ***Left:*** *From top, accumulated moment curves are for* $C_3(z,\ell)$ *with* $\ell = 3, 6, 12$ *and 24 km and for* $C_2(z,\ell)$ *(curves for different scales* ℓ *are all superposed). PDFs are plotted in red, green, blue and pink respectively for* $\ell = 3, 6, 12$ *and 24 km.* ***Right:*** *From top, accumulated moment curves are for* $\ell = 45, 60, 75$ *and 90 km and for* $C_2(z,\ell)$ *(curves for different scales* ℓ *are all superposed). PDFs are plotted in red, green, blue and pink respectively for* $\ell = 45, 60, 75$ *and 90 km. All the PDFs can be compared to the normalized gaussian distribution (pink dashed curve).*

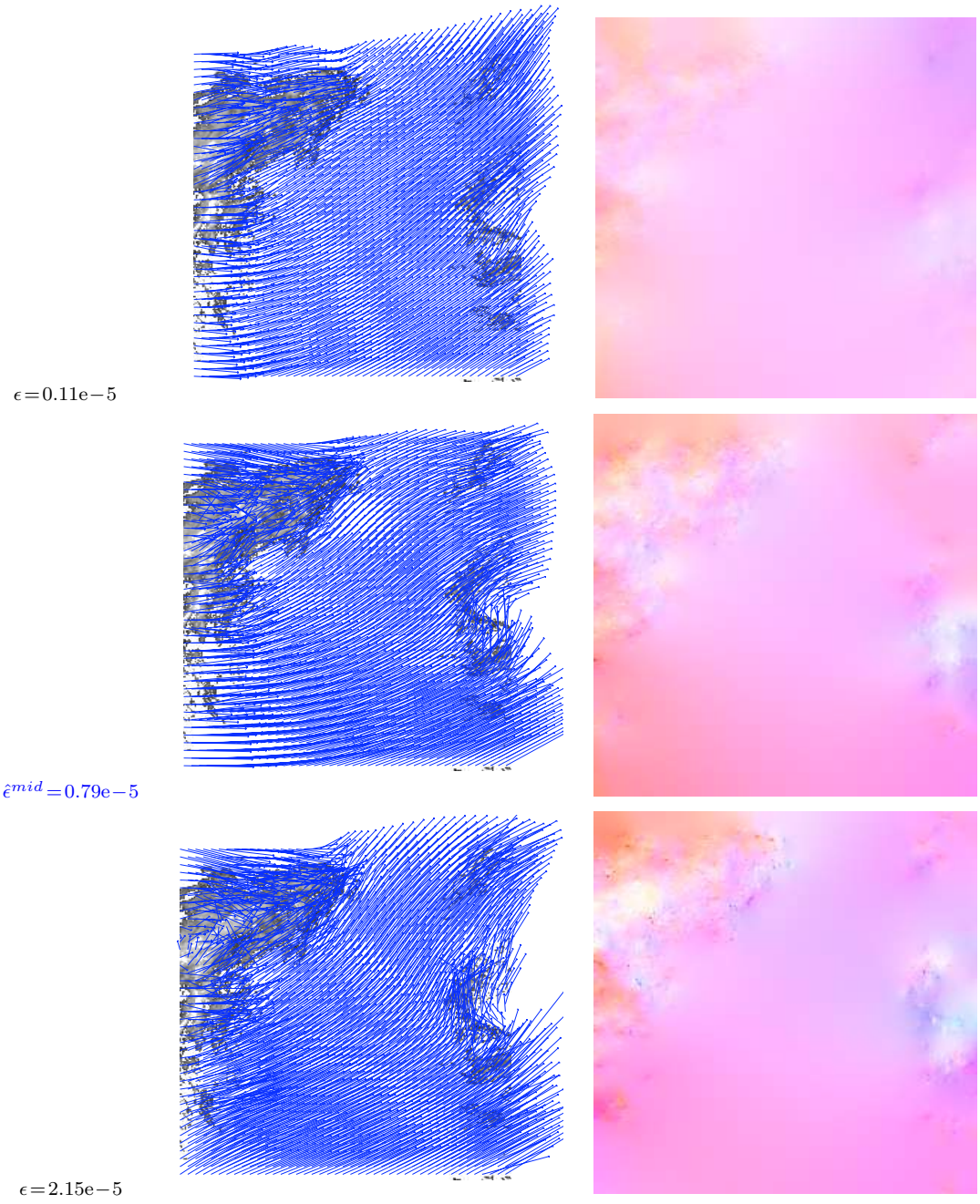

(Heas *et al.*, 2007)

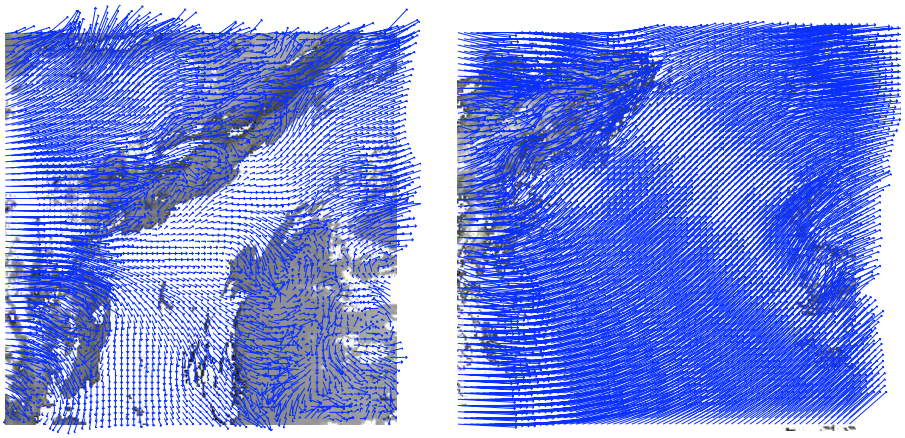

Figure 12: ***Motion at different altitude.*** *Estimated horizontal wind fields at low (left) and intermediate (right) altitude.*

5.2.2 Wind field estimation

Figure 11 displays wind fields at intermediate altitude estimated for different energy fluxes ϵ (*i.e.* different β) which are superimposed on the sparse image observations. Let us remark that the smoothness of the wind field decreases with ϵ. In agreement with the previous spectral comparison, the most likely wind field selected by evidence maximization is much more structured than the estimate provided in (Heas *et al.*, 2007). The latter is displayed for comparison in figure 11. In figure 12, wind field estimated at low and intermediate altitude are displayed. Estimated motions are globally visually consistent. However, motion fields present some local abrupt discontinuities. Most discontinuities seem relevant. Nevertheless, part of them can probably be explained by the weakness of the data model proposed in Heas *et al.* (2007) in areas where the model assumptions are violated (non-layered structures) or by too noisy input observations (due to cloud classification errors, pressure retrieval errors, etc).

6 Conclusions and perspectives

We have presented a physical-based, multi-scale method that does not involve any tuning of regularization parameter for fluid motion modeling in images. It relies on a bayesian hierarchical model which simultaneously provides optimal solutions for two problems: motion estimation and regularization model selection. Regularization models rise from *Kolmogorov*'s theoretical work on turbulent flow self-similarity

and recent results in the study of turbulent flows. Experiments on a synthetic sequence shows that the method is more accurate than the best motion estimators. Moreover, the method constitutes a valuable tool for physical characterization of turbulence from images. In particular, consistent flux across scales in atmospheric turbulence are recovered at different altitudes from a meteorological image sequence.

This work opens interesting perspectives for the experimental measurement of turbulence. Characterizing turbulence cascades could also be performed by analyzing other meteorological images depicting for instance evolution of water vapour or temperature fields. Obviously, this would imply the design of proper direct image observation models. Another interesting perspective could concern the addition of a prior dynamical model to the cinematic consistency obtain with the proposed method. Several works relying on variational image assimilation techniques have recently been led in this direction (Corpetti *et al.*, 2008; N.Papadakis & E.Memin, 2008).

A - Discrete form of the self-similar constraints

Manipulating the derivate of the expectation of Eq. 17 w.r.t motion field $\mathbf{v}$, one obtains for grid points in the subset $\mathbf{S}^\ell$ a new expression for the $\mathbf{s}$-th component of the constraint derivatives $\nabla_{\mathbf{v}} g_\ell(\mathbf{v})$:

$$\nabla_{\mathbf{v}(\mathbf{s})} g_\ell(\mathbf{v}) = \begin{cases} -2\gamma^{-1}\ell^2 \left(D^\ell_{xx} u(\mathbf{s}), D^\ell_{yy} v(\mathbf{s})\right)^T, \text{ if } \ell \in \mathbb{N}^+ \\ -\gamma^{-1}\ell^2 \left(L^\ell_{\frac{\pi}{4}} u(\mathbf{s}) + D^\ell_{xy} v(\mathbf{s}), D^\ell_{xy} u(\mathbf{s}) + L^\ell_{\frac{\pi}{4}} v(\mathbf{s})\right)^T, \text{ if } \ell/\sqrt{2} \in \mathbb{N}^+ \end{cases} \tag{40}$$

where $L^\ell_{\frac{\pi}{4}}$ represents a discrete laplacian operators with a centered 2-nd order finite difference scheme defined on a grid rotated of $\pi/4$ with a mesh equal to ℓ and where D^ℓ_{xx}, D^ℓ_{yy} and D^ℓ_{xy} correspond to the discretization of 2-nd order spatial derivatives in a centered 2-nd order finite difference scheme on a grid with a mesh equal to ℓ.
Considering now the velocity field incremental decomposition $\mathbf{v} = \tilde{\mathbf{v}} + \mathbf{v}'$ used in multi-resolution, as the operator is linear one obtains:

$$\nabla_{\mathbf{v}} g_\ell(\mathbf{v}) \quad = \nabla_{\mathbf{v}} g_\ell(\tilde{\mathbf{v}}) + \nabla_{\mathbf{v}} g_\ell(\mathbf{v}') \tag{41}$$

The constraints can finally be written in their discrete form as:

$$g_\ell(\mathbf{v}) = \frac{1}{2}\mathbf{v}'^T A_\ell \mathbf{v}' - \mathbf{b}_\ell^T \mathbf{v}' + c_\ell = 0, \tag{42}$$

where $A_\ell \mathbf{v}' = \nabla_{\mathbf{v}} g_\ell(\mathbf{v}')$, $\mathbf{b}_\ell = -\nabla_{\mathbf{v}} g_\ell(\tilde{\mathbf{v}})$ and $c_\ell = g_\ell(\tilde{\mathbf{v}})/2$.

B Direct observation model for meteorological images

The physical-based direct observation model presented below has first been introduced in Heas *et al.* (2007). It links a meteorological top of cloud pressure image to a stack of horizontal wind fields.

It is based on the decomposition of the troposphere into a stack of layers at different pressure levels. The k-th layer corresponds to the volume lying in between an upper surface s^{k+1} and a lower surface s^k. These surfaces s^{k+1} are defined by the height of top of clouds belonging to the k-th layer. They are thus only defined only in areas where there exist clouds in the image belonging to the k-th layer,

and remain undefined elsewhere. Cloud classification maps[7] determine the membership of top of clouds to the different layers. Let us denote by C^k the class corresponding to the k-th layer. The associate image of pressure on the top of clouds is used to constitute sparse pressure maps of the layer upper boundaries $p(s^{k+1})$. As with satellite images the lower cloud boundaries are always occluded, we coarsely approximate the missing pressure observations $p(s^k)$ by an average pressure value $\overline{p}(s^k)$ observed on the top of the clouds of the layer underneath. Finally, for the k-th layer, we define sparse image observations I^k corresponding to pressure differences measurements:

$$I^k = \begin{cases} \overline{p}(x,y,s^k) - p(x,y,s^{k+1}) & \text{if} \quad (x,y) \in C^k, \\ \infty & \text{else,} \end{cases} \tag{43}$$

where an infinity value has been assigned to location out of the class.

Such pressure difference images $\{I^k\}$ are used to constitute a precise direct observation model relating the observed pressure measurements to the set of unknown average horizontal motion fields $\{\mathbf{v}^k\}$. For the k-th layer the data term reads:

$$f_d(I^k,\mathbf{v}^k) = \frac{1}{2}\int_\Omega \phi\left((\tilde{I}^k(\mathbf{s}) - I^k(\mathbf{s},t) + \mathbf{v}^k(\mathbf{s})\cdot\nabla\tilde{I}^k(\mathbf{s}) + \tilde{I}^k(\mathbf{s})\mathrm{div}\mathbf{v}^k(\mathbf{s}))^2\right) d\mathbf{s}, \tag{44}$$

where $\phi(.)$ denotes a robust M-estimator such as the Leclerc penalty function (Holland & Welsch, 1977) and $\tilde{I}^k$ denotes the image $I^k(\mathbf{s}, t+\Delta t)$ where the values of pixels out of the class map $C^k(t+\Delta t)$ at time $t+\Delta t$ have been set to zero. Note that in a multiresolution setup, analogously to the linearization of the OFC based data term, a motion-compensate data term is derived by linearization of the previous data functional. Opposite to traditional atmospheric wind field extraction techniques, we are here not relying on cloud luminance patterns seen as passive tracers of the flow (assumption which is known to be violated in some situations) but rather on pressure map evolutions.

References

Abry, P., Gonzales, P. & Flandrin, P. 1995 Wavelets, spectrum analysis and 1/f processes. *Lecture Notes in Statistics: Wavelets and Statistics* **103** (15-29).

Adrian, R. 1991 Particle imaging techniques for experimental fluid mechanics. *Annal Rev. Fluid Mech.* **23**, 261–304.

[7]The EUMETSAT consortium routinely provides such classifications, which are based on thresholds of top of cloud pressure. They also provide top of cloud pressure images of kilometer order.

Baker, S., Scharstein, D., Lewis, J.P., Roth, S., Black, M. & Szeliski, R. 2007 A database and evaluation methodology for optical flow. In *Int. Conf. on Comp. Vis., ICCV 2007*.

Barron, J., Fleet, D. & Beauchemin, S. 1994 Performance of optical flow techniques. *Int. J. Computer Vision* **12** (1), 43–77.

Bergen, J.R., Burt, P.J., Hingorani, R. & Peleg, S. 1992 A 3-frame algorithm for estimating two-component image motion. *IEEE Trans. Pattern Anal. Mach. Intell.* **14** (9), 886–895.

Carlier, J. & Wieneke, B. 2005 Report 1 on production and diffusion of fluid mechanics images and data. *Fluid project deliverable 1.2. http://www.fluid.irisa.fr* .

Charney, J.G. 1971 Geostrophic turbulence. *J. Atmos. Sci* **28**, 1087–1095.

Cho, J. & Lindborg, E. 2001 Horizontal velocity structure functions in the upper troposphere and lower stratosphere 1. observations. *J. Geophysical Research.* **106**, 223–232.

Corpetti, T., Heas, P., Memin, E. & Papadakis, N. 2008 Pressure image assimilation for atmospheric motion estimation. *Tellus A* **61** (3), 160–178.

Corpetti, T., Heitz, D., Arroyo, G., Memin, E. & Cruz, A. Santa 2006 Fluid experimental flow estimation based on an optical flow scheme. *Experiments in Fluids* **40**, 80–97.

Corpetti, T., Mémin, E. & Pérez, P. 2002 Dense estimation of fluid flows. *Pattern Anal Mach Intel* **24** (3), 365–380.

Cuzol, A. & Memin, E. 2007 A low dimensional fluid motion estimator. *Int. J. Computer Vision* **75** (3), 329–349.

Dewan, E. 1997 Saturated-cascade similitude theory of gravity wave spectra. *Journal of Geophysical Research* **102**, 799–818.

Fitzpatrick, J.M. 1988 The existence of geometrical density-image transformations corresponding to object motion. *Comput. Vision, Graphics, Image Proc.* **44** (2), 155–174.

Flandrin, P. 1992 Wavelet analysis and synthesis of fractional brownian motion. *IEEE Trans. on Info. Theory* **38(2)** (910-917).

Frisch, U. 1995 *Turbulence : the legacy of A.N. Kolmogorov*. Cambridge university press.

Gotoh, T., Fukayama, D. & Nakano, T. 2002 Velocity field statistics in homogeneous steady turbulence using a high-resolution direct numerical simulation. *Physics of Fluids* **14**, 1065–1081.

Gull, S F 1989 Developments in maximum-entropy data analysis. In *Maximum Entropy and Bayesian Methods*, pp. 53–71. Kluwer Academic.

Heas, P. & Memin, E. 2008 Three-dimensional motion estimation of atmospheric layers from image sequences. *IEEE trans. on Geo. and Rem. Sensing* **46** (8), 2385–2396.

Heas, P., Memin, E., Papadakis, N. & Szantai, A. 2007 Layered estimation of atmospheric mesoscale dynamics from satellite imagery. *IEEE trans. on Geo. and Rem. Sensing* **45** (12), 4087–4104.

Heitz, D., Heas, P., Mmin, E. & Carlier, J. 2008 Dynamic consistent correlation-variational approach for robust optical flow estimation. *Experiments in Fluids* **45**, 595–608.

Held, M., Wolfe, P. & Crowder, H. P. 1974 Validation of subgradient optimization. *Mathematical Programming* **6**, 62–88.

Holland, P. & Welsch, R. 1977 Robust regression using iteratively reweighted least-squares. *Commun. Statis.-Theor. Meth.* **A6** (9), 813–827.

Horn, B. & Schunck, B. 1981 Determining optical flow. *Artificial Intelligence* **17**, 185–203.

Jaynes, E. T. 2003 *Probability Theory: The Logic of Science*. G. Larry Bretthorst.

J.Pedlosky 1987 *Geophysical Fluid Dynamics*. Springer,New York.

Kolmogorov, A.N. 1941 The local structure of turbulence in inompressible viscous fluid for very large reynolds number. *Dolk. Akad. Nauk SSSR* **30**, 301–5.

Kraichnan, R.H. 1967 Inertial ranges in two-dimensional turbulence. *Phys. Fluids* **10**, 1417–1423.

Kurien, Susan, L'vov, Victor S., Procaccia, Itamar & Sreenivasan, K. R. 2000 The scaling structure of the velocity statistics in atmospheric boundary layer. *Physical Review E (Statistical Physics, Plasmas, Fluids, and Related Interdisciplinary Topics)* **61** (1), 407–421.

Lindborg, E. 1999 Can the atmospheric kinetic energy spectrum be explained by two-dimensional turbulence. *J. Fluid Mech.* **388**, 259–288.

Lindborg, E. & Cho, J. 2001 Horizontal velocity structure functions in the upper troposphere and lower stratosphere 2. theoretical considerations. *J. Geophysical Research.* **106**, 233–241.

Liu, T. & Shen, L. 2008 Fluid flow and optical flow. *Journal of Fluid Mechanics* **614**, 253.

MacKay, David J. C. 1992 Bayesian interpolation. *Neural Computation* **4** (3), 415–447.

MacKay, David J. C. 2003 *Information Theory, Inference, and Learning Algorithms*. Cambridge University Press.

Monin, A.S. & Yaglom, A.M. 1971 *Statistical Fluid Mechanics: Mechanics of Turbulence*. JDover Pubns.

Nastrom, G, Jasperson, W & Gage, K. 1984 Kinetic energy spectrum of large and mesoscale atmospheric processes. *Nature* **310**, 36–38.

N.Papadakis & E.Memin 2008 Variational assimilation of fluid motion from image sequences. *SIAM Journal on Imaging Science, in press* .

Raffel, M., .Willert, C & Wereley, S. 2007 *Particle Image Velocimery A Practical Guide*. Springer.

Taylor, Mark A., Kurien, Susan & Eyink, Gregory L. 2003 Recovering isotropic statistics in turbulence simulations: The kolmogorov 4/5th-law. *PHYSICAL REVIEW E* **2**, 026310.

Tung, Ka Kit 2003 The k 3 and k 5/3 energy spectrum of the atmospheric turbulence: quasi-geostrophic two level model simulation. *J. Atmos. Sci* **60**, 824–835.

Unser, M. 1999 Splines: A perfect fit for signal and image processing. *IEEE Signal Processing Magazine* **16** (6), 22–38.

Weickert, J. & Schnörr, C. 2004 A theoretical framework for convex regularizers in pde-based computation of image motion. *Int. J. Computer Vision* pp. 245–264.

Yuan, J., Schnoerr, C. & Memin, E. 2007 Discrete orthogonal decomposition and variational fluid flow estimation. *Journ. of Math. Imaging & Vison* **28**, 67–80.

Unité de recherche INRIA Rennes
IRISA, Campus universitaire de Beaulieu - 35042 Rennes Cedex (France)
Unité de recherche INRIA Futurs : Parc Club Orsay Université - ZAC des Vignes
4, rue Jacques Monod - 91893 ORSAY Cedex (France)
Unité de recherche INRIA Lorraine : LORIA, Technopôle de Nancy-Brabois - Campus scientifique
615, rue du Jardin Botanique - BP 101 - 54602 Villers-lès-Nancy Cedex (France)
Unité de recherche INRIA Rhône-Alpes : 655, avenue de l'Europe - 38334 Montbonnot Saint-Ismier (France)
Unité de recherche INRIA Rocquencourt : Domaine de Voluceau - Rocquencourt - BP 105 - 78153 Le Chesnay Cedex (France)
Unité de recherche INRIA Sophia Antipolis : 2004, route des Lucioles - BP 93 - 06902 Sophia Antipolis Cedex (France)

Éditeur
INRIA - Domaine de Voluceau - Rocquencourt, BP 105 - 78153 Le Chesnay Cedex (France)
http://www.inria.fr
ISSN 0249-6399